Dynamic and thermodynamic crossover scenarios in the Kob-Andersen mixture: Insights from multi-CPU and multi-GPU simulations*

Daniele Coslovich[a], Misaki Ozawa, and Walter Kob

Laboratoire Charles Coulomb, Université de Montpellier, CNRS, Montpellier, France

Abstract. The physical behavior of glass-forming liquids presents complex features of both dynamic and thermodynamic nature. Some studies indicate the presence of thermodynamic anomalies and of crossovers in the dynamic properties, but their origin and degree of universality is difficult to assess. Moreover, conventional simulations are barely able to cover the range of temperatures at which these crossovers usually occur. To address these issues, we simulate the Kob-Andersen Lennard-Jones mixture using efficient protocols based on multi-CPU and multi-GPU parallel tempering. Our setup enables us to probe the thermodynamics and dynamics of the liquid at equilibrium well below the critical temperature of the mode-coupling theory, $T_{\mathrm{MCT}} = 0.435$. We find that below $T = 0.4$ the analysis is hampered by partial crystallization of the metastable liquid, which nucleates extended regions populated by large particles arranged in an fcc structure. By filtering out crystalline samples, we reveal that the specific heat grows in a regular manner down to $T = 0.38$. Possible thermodynamic anomalies suggested by previous studies can thus occur only in a region of the phase diagram where the system is highly metastable. Using the equilibrium configurations obtained from the parallel tempering simulations, we perform molecular dynamics and Monte Carlo simulations to probe the equilibrium dynamics down to $T = 0.4$. A temperature-derivative analysis of the relaxation time and diffusion data allows us to assess different dynamic scenarios around T_{MCT}. Hints of a dynamic crossover come from analysis of the four-point dynamic susceptibility. Finally, we discuss possible future numerical strategies to clarify the nature of crossover phenomena in glass-forming liquids.

1 Introduction

If a liquid is cooled quickly enough, it will bypass crystallization and form an amorphous solid called glass. Such a glass transition is directly related to the rapid increase of the structural relaxation time upon cooling, whose temperature dependence is given by the Arrhenius law for strong glass-formers and is super-Arrhenius for fragile glass-formers [1]. Despite being purely kinetic in nature, the glass transition is accompanied by a change in the thermodynamic properties of the system at the glass transition temperature T_g. For instance, the specific heat shows a mild increase upon cooling and displays a drop at T_g due to the freezing of the configurational degrees of freedom. Although no phase transition occurs at T_g, it has been suggested that the slowing-down of the dynamics and the resulting glass formation might be driven by a hidden phase transition [2,3].

While most glass-forming liquids follow the trends outlined above, there are notable exceptions. This is the case for instance of liquids with strong, directional interactions, such as silica, silicon, and water. These systems display a thermodynamic anomaly in the form of a local maximum of the specific heat at a temperature $T^* > T_g$ [4], a behavior which has also been observed in simulation studies of silica [5,6], supercooled water [7], and other simple models [8–11]. Concomitantly, also the dynamic behavior of these liquids changes around T^*, crossing over from a super-Arrhenius to an Arrhenius temperature dependence ("fragile-to-strong" crossover). The origin of these thermodynamic and dynamic anomalies has often been attributed to the presence, or proximity, of a liquid-liquid transition or its Widom-line, located at temperatures higher than T_g [4]. Interestingly, this fragile-to-strong crossover is not limited to systems with directional interactions [12]. Recent experimental [13,14] and simulational [15] studies have demonstrated that also several metallic glass-formers exhibit a notable fragile-to-strong crossover. Several interpretations have been proposed to explain the crossover in these systems, including

* Contribution to the Topical Issue "Advances in Computational Methods for Soft Matter Systems" edited by Lorenzo Rovigatti, Flavio Romano, John Russo.

[a] e-mail: daniele.coslovich@umontpellier.fr

the presence of thermodynamic anomalies such as a liquid-liquid transition [15–17], anomalous crystallization [18], or the evolution of structural medium range order [14].

The dynamics of some molecular and polymeric liquids show even a different kind of crossover at a temperature $T_{\rm D}$, typically located about 15%–25% above T_g. This dynamic crossover thus occurs when the relaxation times are around 10^{-8}–10^{-6} s and is subtle, but it can be revealed by temperature-derivative analysis of high-quality dynamic measurements in molecular glass-formers [19–21]. At $T_{\rm D}$ the increase of relaxation times crosses over from super-Arrhenius to a milder temperature dependence and tend to become Arrhenius at very low temperature. While some authors have considered systems with such a crossover as marginal cases [22], an alternative point of view suggests that this behavior may be fairly general [12], even though the location of the crossover is highly system-dependent [20,21].

The physical origin of this dynamic crossover is not completely clear and there are diverging viewpoints on this. Some authors have pointed out the closeness of $T_{\rm D}$ with the temperature at which a power law fit predicts a divergence of the relaxation time data [23,24,12]. The dynamic crossover should then be identified with the critical temperature of the mode-coupling theory (MCT) [25]. Others have attributed this crossover to an upper limit of the activation energy [22,21], which may saturate at an arbitrarily low temperature. While these two interpretations are completely different in nature, they are difficult to disentangle in practice. We emphasize that the dynamic crossover scenario is *a priori* unrelated from one that accompanies liquid-liquid transitions, in that the former does not involve the thermodynamics and is purely dynamic in origin.

Also computer simulations have been used to probe the existence of anomalies in the dynamic and thermodynamic properties of glass-forming liquids. The results of these studies suggest that both the dynamic correlation length scales [26] and the dynamic finite size effects [27] may show a crossover compatible with several theoretical predictions [28–30], although these results do not seem to hold universally. On the other hand, the dynamic range accessible in conventional numerical studies is limited to only 4-5 decades in time. Thus, some of these results might be affected by insufficient equilibration.

In the present study, we focus on a simple glass-former, proposed by Kob and Andersen (KA) [31], that has so far been fairly robust against crystallization and hence has been used in many investigations of the glass transition. Previous studies of this system have given evidence for the presence of a thermodynamic anomaly in the form of a peak in the specific heat [32] and a possible fragile-to-strong crossover [33,34], although these results might have been affected by finite size and finite sampling effects. In the present work we employ an optimized simulation setup, which exploits the parallel tempering method [35] and state-of-art molecular dynamics code running on graphics processing units (GPU), to extend the temperature range in which thermodynamic and dynamic measurements can be done at equilibrium. We find that, in contrast to previous reports [32], the thermodynamics of the liquid is regular. At low temperature, simulations are hindered by crystallization, which involves structures of fcc symmetry formed by large particles. Finally, we discuss possible ways and setups to detect numerically the presence of dynamic anomalies in model glass-formers.

2 Model and methods

2.1 Model parameters

The system we consider is a binary mixture in which both species have the same mass m. The particles interact via a Lennard-Jones potential given by

$$u_{\alpha\beta}(r) = 4\epsilon_{\alpha\beta}\left[\left(\frac{\sigma_{\alpha\beta}}{r}\right)^{12} - \left(\frac{\sigma_{\alpha\beta}}{r}\right)^{6}\right], \qquad (1)$$

where $\alpha, \beta \in \{A, B\}$ are species indices. The value of the parameters $\sigma_{\alpha\beta}$ and $\epsilon_{\alpha\beta}$ are given in ref. [31]. The units of length and energy are set by the parameters $\sigma_{AA} = 1$ and $\epsilon_{AA} = 1$, respectively. The potentials are cut and shifted at a distance $2.5\sigma_{\alpha\beta}$. We simulate systems composed by N particles in a cubic box of side L with periodic boundary conditions and a number density given by $\rho = N/V = 1.1998$. Note that even small differences in density can quantitatively affect the thermodynamic and dynamic observables. For example, in the original paper [31] a different density $\rho = 1.204$ was used, which leads to slight differences in statics and dynamics when sufficiently high-quality data are available. The system size ranges from $N = 300$ to 3600 for parallel tempering simulations (see below). Additional dynamic data have been obtained for a much bigger sample ($N = 100000$) using the LAMMPS simulation package [36,37].

2.2 Simulation protocols

Our simulations implement the parallel tempering (PT) algorithm [35,38], in which M replicas of the system of interest perform independent simulations at temperatures $\{T_i\}$ with the potential energies $\{U_i\}$. At regular intervals, exchanges are attempted between pairs of replicas at neighboring states and the temperatures are exchanged with probability

$$p = \min\left\{1, \exp\left[\left(U_i - U_j\right)\left(\beta_i - \beta_j\right)\right]\right\}, \qquad (2)$$

where $\beta_i = 1/k_{\rm B}T_i$ (with $k_{\rm B} = 1$ in this study), to ensure detailed balance. Since our simulations extend to a temperature range that remained so far largely unexplored, we used different simulation protocols and software to check and validate our results. Namely, we used two independent implementations of the PT algorithm, each one relying on a different molecular dynamics code to carry out the simulation. Note that, for a given system size, we used the same sets of temperatures for all the PT

protocols, namely 0.3730, 0.3810, 0.3901, 0.4003, 0.4115, 0.4238, 0.4374, 0.4525, 0.4692, 0.4877, 0.5082, 0.5307 for $N = 1200$ and 0.4000, 0.4060, 0.4130, 0.4210, 0.4301, 0.4403, 0.4515, 0.4638, 0.4768, 0.4906 for $N = 3600$.

In the first implementation, named PT-1 protocol, we perform multi-CPU parallel tempering simulations with an in-house molecular dynamics code. The MD simulations are performed in the NVT ensemble using the Nose-Hoover thermostat [39] with a time step $\delta t = 0.004$ and a thermostat relaxation time $0.4 = 100\delta t$. We used $M = 12$–14 replicas depending on the system size. The code is parallelized using MPI to handle communications between replicas, which attempt to exchange their state, *i.e.*, the temperature of the associated thermostat, every 50000 MD steps.

The second implementation, named PT-2 protocol, relies on a multi-GPU parallel tempering code [40] that uses the RUMD package [41] as a simulation backend. This multi-GPU code was implemented in python building on the `atooms` framework [42]. Multiple replicas are simulated on individual GPUs and communication between GPUs are handled at high-level via the `mpi4py` package [43]. We ran the multi-GPU simulations on a dedicated cluster of inexpensive gaming cards (GTX-980 and even GTX-750Ti). The thermostat is again of the Nose-Hoover type, the time step is $\delta t = 0.004$ and the thermostat relaxation time $\tau_T = 0.2 = 50\delta t$. We used the same exchange intervals and number of replicas as in PT-1. We checked that increasing the interval between exchanges did not change our results.

Finally, we performed additional PT simulations (PT-3 protocol) to extend our thermodynamic measurements to even lower temperatures than the ones attained by protocols PT-1 and PT-2. The PT-3 simulations are performed using the multi-GPU code described above starting from uncorrelated configurations obtained using the PT-2 protocol at a temperature $T = 0.4$. These efficient multi-GPU simulations enabled us to carefully measure the waiting-time dependence of the results so as to assess equilibration issues, see sect. 3.1.

From these PT simulations, we evaluated the specific heat per particle c_V from the fluctuations of the potential energy U,

$$c_V = \frac{1}{NT^2}\left(\langle U^2\rangle - \langle U\rangle^2\right) + \frac{3}{2}\,, \tag{3}$$

and from the temperature derivative of the average potential energy,

$$c_V = \frac{1}{N}\frac{\partial\langle U\rangle}{\partial T} + \frac{3}{2}\,, \tag{4}$$

where $\langle(\cdots)\rangle$ is the thermal average. The two expressions yield identical results provided the averages are carried out over the equilibrium measure. In a simulation, the agreement between the estimates of c_V obtained through the two methods is often taken as a test of equilibration. We note that, in practice, only very accurate measurements can reveal discrepancies between the two methods. The distributions $P(U/N)$ and the T-dependence of $\langle U\rangle$ obtained from well-equilibrated simulations (PT-3 protocol) are shown in fig. 1.

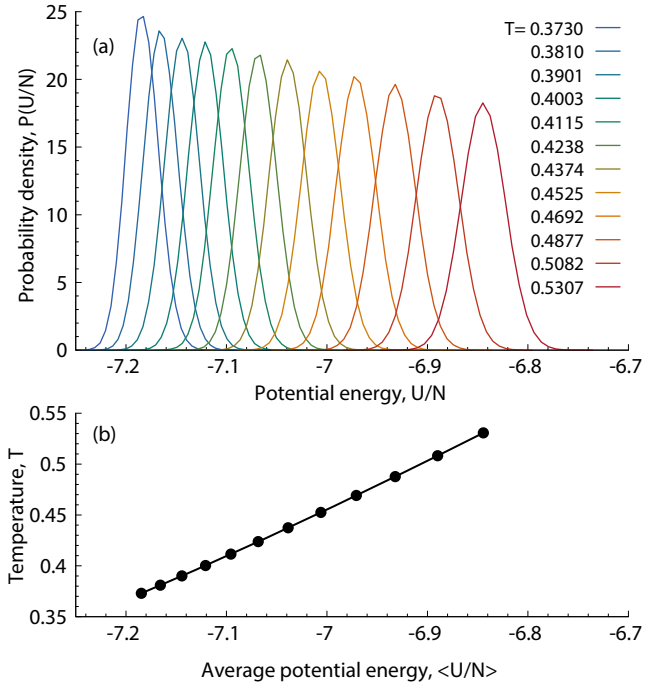

Fig. 1. (a) Distribution of the potential energy per particle $P(U/N)$ for $N = 1200$ obtained from the parallel tempering protocol PT-3. Runs with a substantial fraction of crystalline configurations were discarded from the analysis. (b) Average potential energies per particle for each of the studied temperatures.

Strictly speaking, parallel tempering simulations only give access to thermodynamic and static properties. However, it is possible to perform extended dynamic measurements by starting "regular" simulations from configurations sampled during the PT simulations at a given temperature. Here, again, we follow two distinct protocols to corroborate our results.

In the MC protocol we performed normal Monte Carlo simulations using an in-house code and starting from uncorrelated configurations obtained from protocol PT-1. The MC simulations are carried out in the NVT ensemble using simple displacement moves [44], in which we attempt to displace a randomly selected particles over a cube of side 0.15. We used 10–30 independent configurations depending on temperature. The length of the simulations at the lowest temperature ($T = 0.4$) is 10^9 Monte Carlo steps. In the following, the time unit for the MC protocol is given by one MC sweep, *i.e.*, N attempted displacement moves.

In the MD protocol we performed molecular dynamics simulations using the RUMD package starting from uncorrelated configurations obtained from protocol PT-1 and PT-2. The MD simulations are carried out in the NVT ensemble using the Nose-Hoover thermostat, the time step is $\delta t = 0.004$ and the thermostat relaxation time $\tau_T = 0.2 = 50\delta t$. For the $N = 1200$ samples, we used 128 independent configurations down to $T = 0.4$ from protocol PT-2. For $T = 0.39$, we used only 30 configurations,

namely the final configurations of the PT-2 runs. For the $N = 3600$ samples, we used 20 independent configura-tions from protocol PT-1. The duration t of each of the MD simulations ranged from 4.2×10^6 steps (at $T = 0.51$) to 2.1×10^9 steps (at $T = 0.39$), thus each run was about 10–20 times longer than the typical structural relaxation time τ_α (see below for its definition). In total, for each temperature, our simulations cover over about 2500 structural relaxation times. This high-quality statistics enables us to perform a temperature-derivative analysis of the dynamic data, see sect. 3.2.

For both MC and MD protocols, we checked that the initial configurations were uncorrelated from one another by measuring their mutual self-overlaps [45]

$$Q_{\rm s} = \frac{1}{N} \sum_i \Theta\left(a - |\mathbf{r}_i^\alpha - \mathbf{r}_i^\beta|\right), \qquad (5)$$

where α and β denote two configurations, and their mutual collective overlaps

$$Q_{\rm c} = \frac{1}{N} \sum_{i,j} \Theta\left(a - |\mathbf{r}_i^\alpha - \mathbf{r}_j^\beta|\right). \qquad (6)$$

A sensible choice of parameter a is a fraction of the typical interparticle distance. We chose $a = 0.3$. We found that both $Q_{\rm s}$ and $Q_{\rm c}$ are close to the values expected for uncorrelated pairs of configurations, *i.e.*, $O(1/N)$ and $\frac{4}{3}\pi a^3\rho$, respectively.

From MD and MC simulations we extract the self-part of the intermediate scattering functions

$$F_{\rm s}^A(k,t) = \langle f_{\rm s}^A(k,t)\rangle = \frac{1}{N_A} \sum_j e^{-i\mathbf{k}\cdot[\mathbf{r}_j(t)-\mathbf{r}_j(0)]}, \qquad (7)$$

where the sum runs over the particles of type A. We choose a wave vector $k = 7.25$, close to the first peak of the structure factor [31]. The corresponding structural relaxation time τ_α is defined as usual as $F_{\rm s}^A(k,\tau_\alpha) = 1/e$. In fig. 2, we show the dynamic data obtained from the MD protocol.

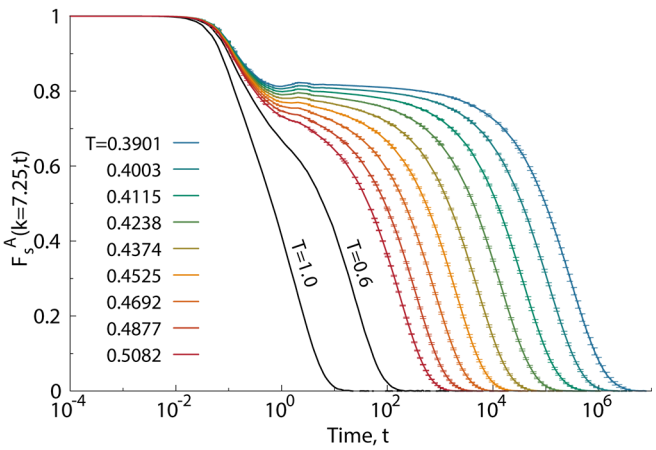

Fig. 2. Self-part of the intermediate scattering functions $F_{\rm s}^A(k,t)$ obtained from the MD protocol for $N = 1200$ particles. Errors bars are one standard deviation on the mean, calculated over 128 runs.

2.3 Crystalline order detection

The study of glass-forming liquids is often hampered by crystallization and the very relation between glassy behavior and crystallization remains a matter of debate [46, 47]. The KA mixture, which is a simple model of a metallic glass-former, has been extensively used as a model to study the glass transition because of its stability against crystallization. Until very recently, the note added in the proofs of ref. [48] was, to the best of our knowledge, the only report of crystallization of this model by direct simulation, achieved through runs of about 3.7×10^7 time units (7.4×10^9 steps) at $T = 0.40$. At this temperature, however, the nucleation time is still much larger than the structural relaxation time τ_α ($\sim 10^5$ time units), and therefore MD/MC simulations of the metastable liquid can be carried out safely. In this work, however, we were able to equilibrate the mixture at even lower temperatures. Below $T = 0.4$, crystallization events become increasingly frequent, as also demonstrated by a very recent simulation study [49]. Within the studied range of system sizes, the smaller the system, the stronger the tendency to crystallization.

As a first indicator of crystallization events in our simulations, we monitored the evolution of the inherent structure (IS) energy as a function of time [50]. However, the IS energy may also display large but reversible fluctuations, unrelated to crystal nucleation. We thus studied two additional order parameters that allow us to disentangle "amorphous" and crystalline fluctuations. The first one relies on the so-called common neighbor analysis (CNA) [51]. In this approach, the bonds formed by neighboring particles are classified according to the number of shared neighbors. It has been shown that the fraction f_{142} of bonds of type 142, see, *e.g.*, ref. [52], allows one to detect crystallization in *biased* simulations of the KA mixture. We found that this approach allows one to detect crystallization in the bulk mixture as well. An example of a crystallization event is depicted in fig. 3. Even though the nature of the fluctuation is not always clear-cut, we found that a threshold on f_{142} is an effective criterion to filter out crystalline configurations. Note that since we run several replicas at a time, only a few of them may be affected by crystallization. When this occurs they typically remain "stuck" in the lowest portion of temperature space. As in ref. [52], we used a threshold of 12% CNA-142 bonds. A large crystalline cluster detected in our simulations is shown in fig. 3(d). The crystal nucleus is formed by fcc pockets of A particles, which implies compositional fluctuations that deplete B particles. To detect it, we introduced an even simpler order parameter, namely the concentration of cages formed by A particles only [52]. In particular, we evaluated the connected component [53] of clusters formed by pure-A cages. We found that in typical crystalline samples, the size of these connected clusters is about a few hundred particles. Finally, in fig. 3(c) we show

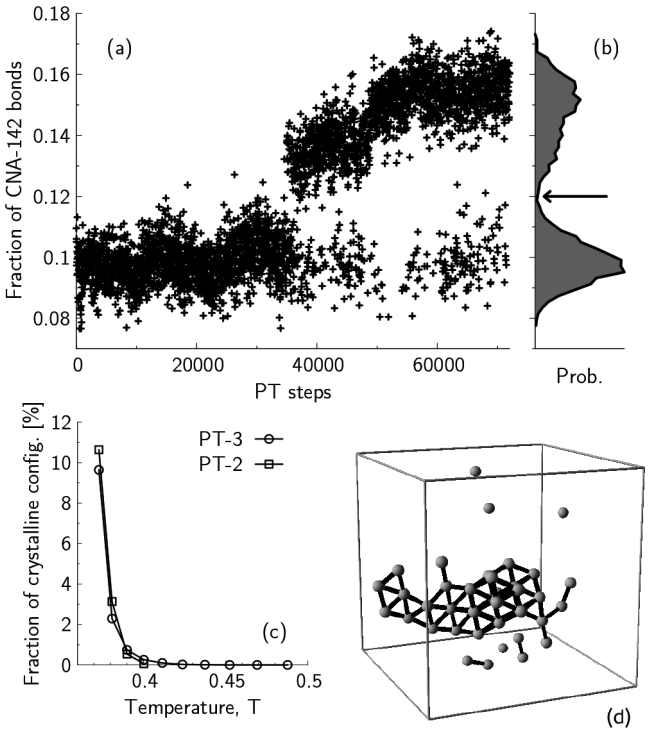

Fig. 3. Detection of crystalline configurations. (a) Crystallization event during a PT-2 simulation for $N = 1200$ particles. The fraction of CNA-142 bonds, f_{142}, is shown as a function of PT steps (1 PT step=50000 MD steps). (b) The probability density calculated during the run shows a bimodal distribution with a sharp minimum around $f_{142} \approx 12\%$. (c) Percentage of crystalline configurations, detected using a 12% threshold on f_{142}, as a function of temperature. Below $T = 0.4$, both PT-2 and PT-3 protocols have a large fraction of crystalline configurations. PT-2 data were not analyzed above $T = 0.4$. (d) Connected component of a cluster formed by particles surrounded by A particles only during a crystallization event.

the percentage of crystalline configurations in the simulations of protocol PT-2 and PT-3 for $N = 1200$ particles. We see that they increase markedly below $T = 0.4$. To deal with data analysis in this delicate regime while retaining the maximum possible amount of statistics, we filtered our c_V measurements by discarding individual configurations whose CNA-142 concentration was higher than 0.12, see sect. 3.1. On the other hand, above $T = 0.4$ the fraction of samples above the crystalline threshold is negligible and we rarely encountered problematic runs. These runs were simply discarded all together.

3 Results

3.1 Thermodynamics

The specific heat c_V is a sensitive, although not unambiguous, indicator of thermodynamic changes in dense liquids. For instance, a sudden drop in c_V as a function of the control parameters may be due to a phase transition, or more generally to a change in the topography of the underlying energy landscape, but might as well indicate incomplete equilibration, as is the case at the laboratory glass transition observed upon cooling. Previous work on the KA mixture showed the presence of a peak in c_V at some temperature close to the mode-coupling temperature $T_{\rm MCT} = 0.435$ [31]. In this section, we show that the thermodynamics of the KA mixture is regular, *i.e.*, it shows no anomaly, at least down to $T = 0.39$ and that the peak found in ref. [32] is due to partial equilibration. Below $T = 0.4$, equilibration becomes hard on current simulation time scales and analysis is further hampered by crystallization events. Finally, we discuss the possible presence of a thermodynamic anomaly in this highly metastable portion of the phase diagram.

In fig. 4(a) we show specific heat measurements from parallel tempering simulations using protocols PT-1 and PT-2. We also include results from a previous study using PT simulations, which reported a peak in c_V around $T_{\rm MCT}$ [32]. From our data, we conclude that no anomaly is observed in the specific heat, which increases monotonically down to $T = 0.39$. The length of our simulations is typically one order of magnitude longer than those of ref. [32]. In retrospect, our work warns that tests such as histogram reweighting or the consistency of fluctuation and derivative expressions of response functions, such as c_V, are not sufficient to ensure equilibration of supercooled liquids, see ref. [54] for a more detailed discussion of this issue. Also, our results imply that one needs at least $\sim 10^9$ MD time steps to equilibrate the KA mixture below $T_{\rm MCT}$.

The empirical model of Rosenfeld-Tarazona [55] proposes the following functional form for the potential energy $U = aT^{3/5} + b$, which yields $c_V \sim T^{-2/5}$. In fig. 4(b) we draw the specific heat data from protocols PT-1 and PT-2 as a function of $T^{-2/5}$, which linearizes the Rosenfeld-Tarazona law. A similar representation yields an excellent data collapse for simple liquids in both normal and moderately supercooled regime [56]. We find that this functional form provides a very good description of the data but a slight upward bending is observed around $T = 0.4$, suggesting the presence of additional fluctuations not accounted for by this simple liquid-state model. This is confirmed by the analysis of the third moment of the potential energy distribution. We found that the skewness remains constant at high temperature and starts to increase slightly around $T = 0.4$ (not shown), even when crystalline configurations are removed from the analysis. This behavior may be thus attributed to crystallization precursors or to enhanced fluctuations of the locally favored structure of the system [57,58].

We found that the measurements using PT-1 and PT-2 start to deviate significantly from each other below $T = 0.39$. Moreover, in this temperature regime, the liquid has an increased tendency to crystallize, see sect. 2. In fig. 4(c) we show measurements of c_V from protocol PT-3, in which crystalline samples are removed on a per-configuration basis and equilibration is assessed directly, *i.e.*, by measuring the waiting-time dependence of c_V. Specifically, we start parallel tempering simulations from previously equilibrated configurations at $T = 0.4$ and per-

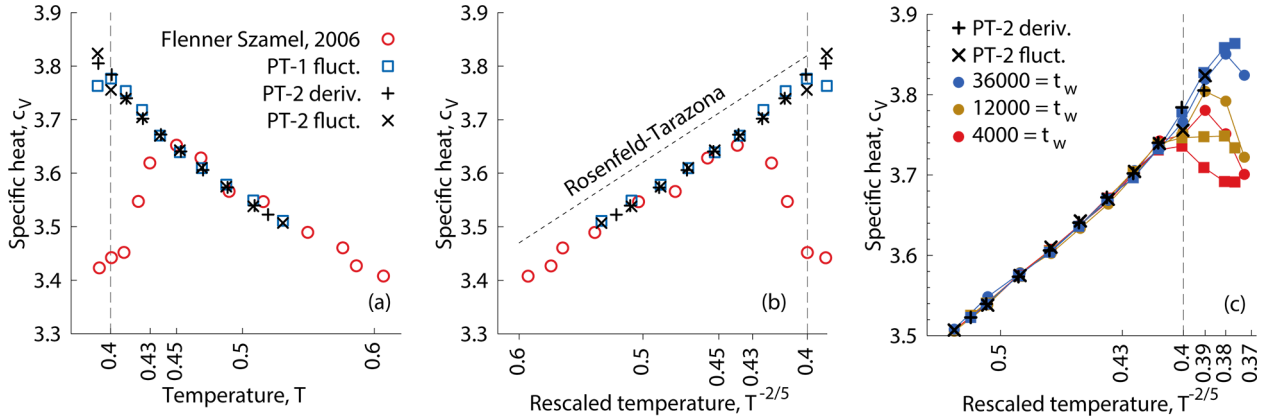

Fig. 4. (a) Specific heat from protocols PT-1 and PT-2 for $N = 1200$ particles in the regime $T \gtrsim 0.4$ where crystallization is negligible. Results from fluctuation and derivative expressions of the specific heat are shown as indicated in the legend. The temperature of the data from ref. [32] (circles) is divided by the density scaling factor $(1.204/1.2)^{\gamma}$, with $\gamma = 5.0$ to correct for the small density mismatch. (b) Rosenfeld-Tarazona scaling of the same specific heat c_V data as in panel (a). (c) Specific heat from protocol PT-3 for different waiting times t_w expressed in unit of PT steps. Results from fluctuation and derivative expressions of the specific heat correspond to circles and squares, respectively. Configurations with $f_{142} > 0.12$ are discarded from the calculations.

form averages over restricted portions of the trajectories as follows:

$$\langle A \rangle_{t_w} = \frac{1}{t_p - t_x} \int_{t_w}^{t_w + t_p} \mathrm{d}t A(t) W(t), \qquad (8)$$

where t_w is the waiting time and $W(t) = \Theta(0.12 - f_{142})$ is a windowing function that removes from the averages samples identified as crystalline (see sect. 2) and $t_x = \int_{t_w}^{t_w+t_p} \mathrm{d}t(1-W(t))$. The production time t_p was kept fixed to 36000 PT steps, independently of waiting time.

In fig. 4(c) we show the results obtained by calculating the specific heat starting from time t_w with increasing values of t_w. We emphasize that these specific heat measurements cover a temperature regime that has never been probed before at equilibrium. For temperatures higher than 0.4, the results of the PT-3 protocol show a consistent, *i.e.*, t_w-independent, growth of c_V, thus corroborating our previous analysis. Below $T = 0.4$, the specific heat measurements display a more marked waiting-time dependence but fluctuation and derivative formulas converge for sufficiently long waiting times and reveal a monotonic increase of c_V down to $T = 0.38$. Only at the lowest temperature, the specific heat c_V measured from energy fluctuations shows a local maximum. The dependence of this peak as a function of waiting time suggests that this feature may be actually due to lack of equilibration.

Recent simulations based on trajectory path sampling [58] suggest the existence of a liquid-liquid transition in the low temperature part of the phase diagram of the KA mixture. Our data narrow down the temperature range over which this hypothetical transition may occur and rule out thermodynamic anomalies for $T > 0.37$. These results do not exclude, however, the scenarios discussed in ref. [58]. Given the strong tendency to crystallize below $T = 0.4$, however, our results show that a thermodynamic anomaly, if present at all in the KA mixture, is hidden in a highly metastable portion of the phase diagram. In practice, it will be very difficult to detect it in large enough samples. Therefore, we think that future work in this context should focus on more robust models of glass-formers.

3.2 Dynamics

The parallel tempering algorithm allows one to accelerate the sampling of static and thermodynamic observables, but it does not provide by itself useful information on the dynamics. However, it is possible to carry out dynamic measurements by using uncorrelated configurations extracted from PT simulations as starting points of conventional molecular dynamics or Monte Carlo simulations. This approach can be parallelized in a trivial way by performing independent simulations and allows one to extend the accessible dynamic range by short-circuiting equilibration issues. In this section, we implement these ideas following using the MD and MC protocols described in sect. 2 and test various dynamic crossover scenarios below the MCT temperature.

Figure 5(a) shows an Arrhenius representation of the relaxation times obtained using the MD and MC protocols for 1200 and 3600 particles. We note that equilibrium sampling is ensured by the fact that both MD and MC simulations start from previously equilibrated configurations down to $T = 0.39$. The time scale of Monte Carlo simulations has been scaled to match the relaxation times of MD at low temperature. We also include dynamic data from ref. [57], which agree with the new set of simulations over the common temperature range. Very similar behavior is found also for B-type particles (not shown). Thanks to the hybrid protocols employed in the present work, the accessible dynamic range has increased by almost two orders of magnitude compared to the conventional molecular

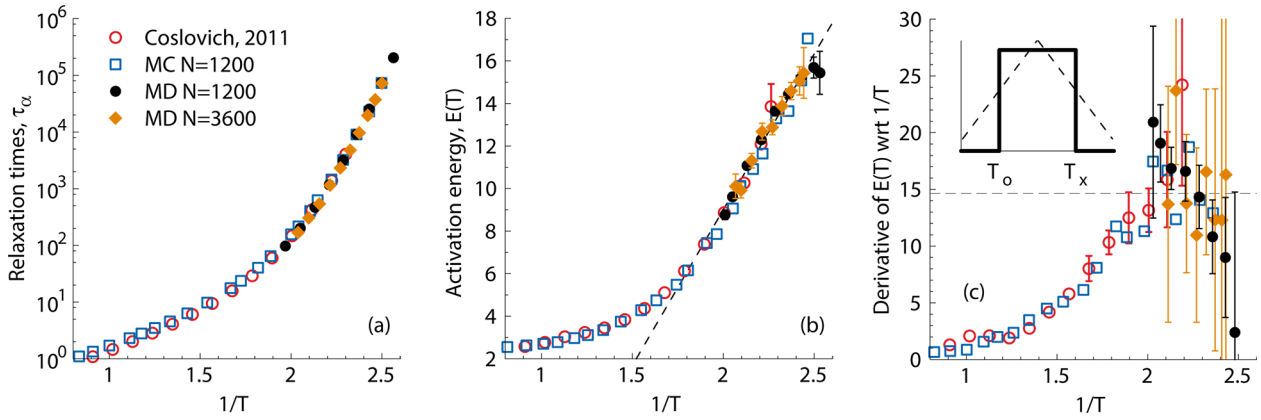

Fig. 5. Temperature-derivative analysis of relaxation times. The relaxation times obtained from MC simulations have been scaled by 5×10^2 MC steps. Error bars on MD data represent one standard deviation on the mean and are only shown when larger than the symbol size. (a) Relaxation times τ_α as a function of $1/T$ for various protocols and system sizes. (b) Activation energy $E(T)$ for the same set of data as panel (a). The dashed line indicates a linear fit to eq. (11) in the range $T \leq 0.52$ with $J = 2.7$ and $T_0 = 0.72$. (c) Derivative of $E(T)$ with respect to $1/T$. The horizontal line corresponds to $2J^2$. The inset shows a schematic representation of two possible scenarios for this derivative: the solid line depicts the behavior expected from facilitation models, while the dashed line is the qualitative behavior described in ref. [21].

dynamics simulations of ref. [57] and we can comfortably study the dynamics below $T_{\rm MCT}$. The data suggest that the temperature dependence of the relaxation times gets milder, *i.e.*, more Arrhenius like, at the lowest temperatures. However, it is notoriously difficult to draw firm conclusions based on analysis of the relaxation time alone, which has led to a number of controversies [12].

Temperature-derivative analysis of the dynamic data provides a most stringent test of analytic expressions for $\tau_\alpha(T)$ and is particularly well-suited to reveal the presence of a dynamic crossover [19–21]. Even though this approach requires very accurate data, it has the advantage of being parameter free and requires no data fitting. So far, it has mostly been applied to high-quality dielectric relaxation measurements. To the best of our knowledge, the only numerical study to conduct this analysis across the MCT temperature is ref. [59] for a mixtures of harmonic spheres. Here, we push this kind of analysis even further by combining the trivial parallelism of our MD and MC protocols and the efficiency of the RUMD simulation package on small system sizes [41].

The central quantity in our analysis is the apparent activation energy

$$E(T) = \frac{\mathrm{d} \ln \tau_\alpha}{\mathrm{d}(1/T)}, \tag{9}$$

which we compute by the centered difference method[1]. A graph of $E(T)$ *versus* $1/T$ provides a simple way to test the parabolic law proposed by Elmatald *et al.* [22] in the context of dynamic facilitation

$$\tau_\alpha = \tau_0 \exp\left[\left(\frac{J}{T_0}\right)^2 \left(\frac{T_0}{T} - 1\right)^2\right], \tag{10}$$

where τ_0, J, and T_0 are material parameters. The activation energy is then a linear function of $1/T$ given by the following expression:

$$E_p(T) = \frac{2J^2}{T_0}\left(T_0/T - 1\right). \tag{11}$$

It should be emphasized that eq. (10) is only expected to hold below the onset temperature T_0 and above an additional reference temperature T_x. Outside this range of temperatures, the dynamics is expected to be Arrhenius [22].

A similar approach can be used to linearize the classic VFT equation. Following Stickel *et al.* [19] we introduce $\phi = E(T)^{-1/2}$. By computing the derivative of the VFT expression

$$\tau_\alpha = \tau_0 \exp\left[\frac{T_{\rm vft}}{K(T - T_{\rm vft})}\right], \tag{12}$$

we obtain

$$\phi(T) = \sqrt{\frac{K}{T_{\rm vft}}}\left(1 - \frac{T_{\rm vft}}{T}\right), \tag{13}$$

where τ_0, K, and $T_{\rm vft}$ are parameters. Thus, the VFT equation appears linear in a graph where ϕ is shown as a function of $1/T$ [19].

In fig. 5(b) we show $E(T)$ as a function of $1/T$. Overall, the activation energy displays an approximately linear behavior at sufficiently low temperature, *i.e.*, $T < 0.5$. This behavior is well captured by eq. (11), although fitting the relaxation times in this range requires a value

[1] Given a set $\{x_i\}$ of points and corresponding function values $\{f_i\}$, with $0 \leq i \leq M$, we compute the derivative at $(x[i+1]+x[i-1])/2$ as $(f[i+1]-f[i-1])/(x[i+1]-x[i-1])$ if $0 < i < M$. We use $(f[1] - f[0])/(x[1] - x[0])$ and $(f[M]-f[M-1])/(x[M]-x[M-1])$ for the first and last pairs of points, respectively. The expression used at the boundaries is more noisy than the one for $0 < i < M$.

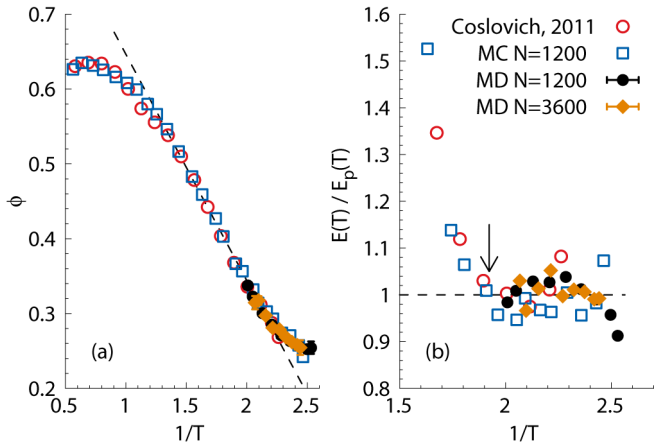

Fig. 6. Critical assessment of the VFT and parabolic laws. (a) Stickel plot $\phi(T)$ *versus* $1/T$. (b) Plot of $E(T)/E_p(T)$ as a function of $1/T$. The dashed lines are guides to the eye. The arrow indicates the temperature $T = 0.52$ from which the parabolic law begins to apply.

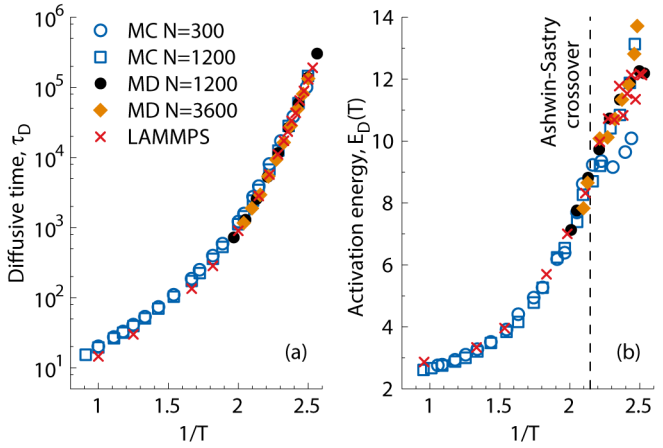

Fig. 7. Analysis of diffusive times τ_D. The diffusive times obtained from MC simulations have been scaled by 5×10^2 MC steps. (a) Arrhenius representation of the diffusive times τ_D. (b) Activation energies from the diffusive time τ_D. The vertical line indicates the crossover observed by Ashwin and Sastry in ref. [33] for a system of 256 particles.

$T_0 \approx 0.72$, which is lower than the usual estimates 0.8–1.0, see, *e.g.*, ref. [60], but consistent with a very recent analysis [61] based on eq. (11). We also note that the value of $J/T_0 = 3.7$ is larger than the one used in ref. [22]. The fit parameters used in ref. [22] appear to strike a balance between the high and low T portions of the data. For the most accurate data set, *i.e.*, MD with $N = 1200$, and at the lowest temperatures, this representation also reveals a slight inflection in $E(T)$. This slight saturation may suggest a dynamic crossover similar to the one observed in certain molecular glass-formers [62] and in the simulation of harmonic spheres [59]. One comment on possible finite size effects is in order. In a small sample, the activation energy necessarily reaches an upper bound and a smooth crossover to Arrhenius behavior is expected at a system-size–dependent temperature [63]. Within the quality of our data the temperature dependence for different system sizes gives compatibles results. However, due to the larger scatter in the $N = 3600$ samples, we cannot completely rule out the possibility that the inflection of the $N = 1200$ is due to a finite size effect.

Pushing our analysis one step further, we compute the derivative of $E(T)$ with respect to $1/T$ and show the results in fig. 5(c). This quantity should be constant and equal to $2J^2$ in the dynamic facilitation scenario, whereas other models [62] predict that it should peak around some crossover temperature. The inset of the figure illustrates schematically these two possible scenarios. Within the noise of the data, and in particular of our most accurate data set (MD with $N = 1200$), our measurements are compatible with a decrease of $\mathrm{d}E(T)/\mathrm{d}(1/T)$ below some temperature T_D close to T_MCT. Simulations at even lower temperature and better statistics for larger system sizes would be needed to fully confirm this behavior.

In fig. 6(a) we test the validity of the VFT law by computing $\phi(T)$ as a function of $1/T$. We find that the VFT law holds well at intermediate temperatures, but clear deviations are visible at low temperature. This confirms the well-known observation [19] that, except in rare cases, the VFT equation cannot describe the full T-dependence of the dynamic data. In fig. 6(b) we show a plot $E(T)/E_p(T)$ *versus* $1/T$. In this representation, the parabolic law would correspond to a horizontal line. We see that the data flatten out only below $T = 0.52$, thus the range over which this law holds in the KA mixture is actually more limited than previously thought [22].

We also computed the activation energy E_D from the diffusive time τ_D, defined as the time needed to reach a mean square displacement of A particles equal to 1. These diffusive times are shown in fig. 7(a) for several protocols and system sizes. We then compute, as before, the activation energies E_D associated to diffusive times τ_D. Figure 7(b) indicates that the growth of E_D gets milder below some crossover temperature $T_\mathrm{D} \simeq 0.45$. Again, our $N = 1200$ MD data-set suggests an inflection of E_D around this temperature. This crossover temperature is remarkably close to the one reported long ago by Ashwin and Sastry in ref. [33] for a smaller system size ($N = 256$). However, in small systems E_D actually saturates at T_D, while bigger samples only cross over to a milder temperature dependence. These results indicate that, even though the results of ref. [33] were probably affected by finite size effects, the diffusion mechanism might actually change in a temperature range close to the MCT transition temperature. This is corroborated by the analysis of a much larger sample ($N = 100000$) simulated using LAMMPS, which gives a trend compatible with the ones observed for $N = 1200$ and $N = 3600$ particles. These large-scale simulations were performed in the NVT simulations using the Nose-Hoover thermostat but without parallel tempering.

Finally, we compute the dynamic fluctuations associated to the time-dependent self-overlap function

$$Q_\mathrm{s}(t) = N^{-1} \sum_j \Theta(0.3 - |\mathbf{r}_j(t) - \mathbf{r}_j(0)|), \qquad (14)$$

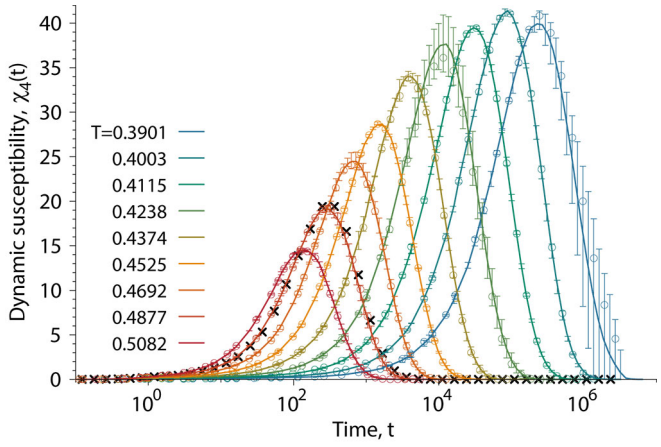

Fig. 8. Dynamic susceptibility $\chi_4(t)$ from MD protcol (NVT ensemble) for $N = 1200$ particles. The full lines are measurements over the entire length of the runs, while the symbols are measurements restricted to the first half of the runs. The error bars are estimated from the difference between the first and second halves of the runs. The crosses correspond to $\chi_4^{NVE}(t) + T^2(\frac{\mathrm{d}Q_\mathrm{s}}{\mathrm{d}T}(t))^2/c_V$, see eq. (16), at $T = 0.4877$.

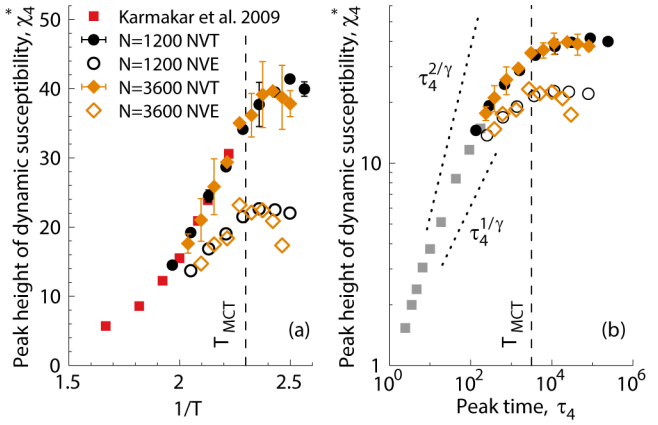

Fig. 9. Peak height of the dynamic susceptibility χ_4^* in the NVT ensemble (full symbols) and in the NVE ensemble (empty symbols) as a function of (a) $1/T$ and (b) the peak time τ_4. The vertical line in the two panels marks the MCT temperature. The dotted lines in panel (b) indicate the predicted MCT scaling in the NVT (exponent $2/\gamma$) and NVE ensemble (exponent $1/\gamma$). Squares in panel (a) are taken from ref. [66]. Squares in panel (b) indicate results from additional, high-temperature NVT simulations for $N = 1200$ particles.

where the sum is taken over all particles. The dynamic susceptibility is then defined as

$$\chi_4(t) = N\left\{\left[\langle Q_\mathrm{s}(t)^2\rangle\right] - \left[\langle Q_\mathrm{s}(t)\rangle\right]^2\right\}, \qquad (15)$$

where $[\ldots]$ indicates an average over statistically independent initial samples and $\langle\ldots\rangle$ a time average over a given run. The dynamic susceptibilities, shown in fig. 8 for $N = 1200$, display a peak at a time τ_4 proportional to the structural relaxation time. The peak height χ_4^* is a standard proxy for the extent of dynamic heterogeneity in supercooled liquids [3].

In figs. 9(a) and (b) we show χ_4^* as a function of $1/T$ and as a function of τ_4^*, respectively. The dynamic fluctuations quantified by the susceptibility in the NVT ensemble cross over around the MCT temperature to a very mild dependence on both temperature and relaxation time. Within the quality of our data, this effect *cannot* be attributed to the finite size of the system. We point out, however, that the MCT scaling expected in the NVT ensemble [64], $\chi_4^* \sim \tau_\alpha^{\gamma/2} \sim \tau_4^{\gamma/2}$, where $\gamma \approx 2.4$ is the exponent of power law fit to the relaxation time, does not hold well for this system. Therefore, the fact that the crossover in the dynamic susceptibility occurs close to the mode-coupling temperature may be coincidental. We also note that similar results may not hold for the full dynamic susceptibility [3], which includes contributions from number fluctuations and which we have neglected here. Our results resonate with those of Flenner and Szamel [65], who showed that some contributions to the total susceptibility, notably those associated to dynamic fluctuations in the NVE ensemble, may be more sensitive to the presence of a crossover than the full susceptibility. To address this point quantitatively, we computed the dynamic susceptibility in the NVE ensemble from the exact expression [67]

$$\chi_4^{NVE}(t) = \chi_4^{NVT}(t) - \frac{T^2}{c_V}\left(\frac{\mathrm{d}Q_\mathrm{s}}{\mathrm{d}T}(t)\right)^2. \qquad (16)$$

We checked that the above expression yields results consistent with those obtained from simulations in the NVE ensemble at $T = 0.4877$, at which the energy drift during NVE simulations was not too severe, see fig. 8. The temperature dependence of the peak height of $\chi_4^{NVE}(t)$, shown in fig. 9, provides clear hints of a dynamic crossover around the MCT temperature and corroborates the findings of ref. [65]. Royall *et al.* [68] have also noted that the growth of χ_4^* observed in simulations at above T_MCT is incompatible with the typical correlation lengths measured experimentally. From this point of view, our finding of a crossover to a much milder rate of growth of dynamic correlations is a welcome result, which may solve the apparent conundrum evidenced in ref. [68].

4 Conclusions

In this work we have performed extensive computer simulations to probe the existence of thermodynamic and dynamic anomalies in the Kob-Andersen binary Lennard-Jones mixture. Our simulations build on an efficient simulation setup, which combines algorithmic and hardware optimizations. In particular, we exploit the parallel tempering algorithm and multi-GPU acceleration to measure the specific heat at equilibrium down to unprecedented temperatures. We also appreciably extend the range of dynamic measurements by starting regular MD and MC simulations from independent configurations

previously equilibrated with parallel tempering. This approach is trivially parallel and enables us to perform a temperature-derivative analysis of the dynamic data.

Thanks to these advances, we could clarify some is-sues related to the thermodynamic and dynamic behavior of the mixture. In particular, we found that the specific heat increases monotonically down to at least $T = 0.38$, in contrast with previous findings [32], which suggested a maximum around $T = 0.43$ and which was proba-bly due to out-of-equilibrium effects. Although crystalliza-tion renders the analysis difficult at low temperature, our data indicate that thermodynamic anomalies, if present at all, must occur in a highly metastable, low-temperature portion of the phase diagram. Conversely, any possible crossover above $T = 0.38$ must be purely dynamic in ori-gin. By performing a temperature-derivative analysis of the dynamic data and by analyzing the dynamic susceptibilities, we have assessed several scenarios that may involve a dynamic crossover in this temperature regime. One possible scenario suggests the presence of a crossover [27, 30] around the mode-coupling temperature T_{MCT}. There are, however, alternative interpretations that attribute the dynamic crossover to a saturation of energy barriers, as is the case in elastic models [69, 70], free-volume models [71] and even possibly in the dynamic facilitation scenario at sufficiently low temperature [72]. In these latter scenarios, the crossover need not be around T_{MCT}.

Although our analysis is not entirely conclusive yet, we argue that state-of-the-art simulation methods com-bined with temperature-derivative analysis of simulation data may hold the key to fully disentangle these sce-narios in the near future. Judging from the quality of our temperature-derivative analysis and dynamic fluctua-tions measurements, we infer that simulations of the or-der of several thousands of structural relaxation times are needed to fully confirm or rule out the presence of dy-namic crossovers. Our results also suggest that contribu-tions to the dynamic susceptibility measured in ensembles where conserved quantities are not free to fluctuate may better probe the dynamic behavior than the full suscep-tibility [64]. For specific systems, specialized Monte Carlo moves, like particle swaps [73–77], may provide an ad-ditional and important efficiency improvement and facili-tate thermodynamic and dynamic studies below the mode-coupling temperature.

We thank E. Flenner and G. Szamel for useful discussions. We acknowledge PRACE for awarding us access to Curie at GENCI@CEA, France, which enabled the development of part of the software used in this work. Data relevant to this work can be accessed at `https://doi.org/10.5281/zenodo.1227831`.

Author contribution statement

The simulations were performed as follows: protocol PT-1 and LAMMPS by WK, protocol PT-2, PT-3, and MD by DC and MC by MO. DC and MO analyzed the data. DC wrote the first draft of the article. All authors discussed the results and contributed to the final manuscript.

References

1. C.A. Angell *et al.*, Science **267**, 1924 (1995).
2. K. Binder, W. Kob, *Glassy Materials and Disordered Solids: An Introduction to Their Statistical Mechanics* (World Scientific, 2011).
3. L. Berthier, G. Biroli, Rev. Mod. Phys. **83**, 587 (2011).
4. C.A. Angell, MRS Bull. **33**, 544 (2008).
5. P. Scheidler, W. Kob, A. Latz, J. Horbach, K. Binder, Phys. Rev. B **63**, 104204 (2001).
6. I. Saika-Voivod, F. Sciortino, P.H. Poole, Phys. Rev. E **69**, 041503 (2004).
7. S. Saito, I. Ohmine, B. Bagchi, J. Chem. Phys. **138**, 094503 (2013).
8. A.J. Moreno, S.V. Buldyrev, E. La Nave, I. Saika-Voivod, F. Sciortino, P. Tartaglia, E. Zaccarelli, Phys. Rev. Lett. **95**, 157802 (2005).
9. L. Xu, S.V. Buldyrev, N. Giovambattista, C.A. Angell, H.E. Stanley, J. Chem. Phys. **130**, 054505 (2009).
10. R. Gutiérrez, S. Karmakar, Y.G. Pollack, I. Procaccia, EPL **111**, 56009 (2015).
11. M. Ozawa, K. Kim, K. Miyazaki, J. Stat. Mech. Theory Exp. **2016**, 074002 (2016).
12. F. Mallamace, C. Branca, C. Corsaro, N. Leone, J. Spooren, S.H. Chen, H.E. Stanley, Proc. Natl. Acad. Sci. U.S.A. **107**, 22457 (2010).
13. C. Zhang, L. Hu, Y. Yue, J.C. Mauro, J. Chem. Phys. **133**, 014508 (2010).
14. C. Zhou, L. Hu, Q. Sun, H. Zheng, C. Zhang, Y. Yue, J. Chem. Phys. **142**, 064508 (2015).
15. K.N. Lad, N. Jakse, A. Pasturel, J. Chem. Phys. **136**, 104509 (2012).
16. S. Wei, F. Yang, J. Bednarcik, I. Kaban, O. Shuleshova, A. Meyer, R. Busch, Nat. Commun. **4**, 2083 (2013)
17. M. Stolpe, I. Jonas, S. Wei, Z. Evenson, W. Hembree, F. Yang, A. Meyer, R. Busch, Phys. Rev. B **93**, 014201 (2016).
18. X. Yang, C. Zhou, Q. Sun, L. Hu, J.C. Mauro, C. Wang, Y. Yue, J. Phys. Chem. B **118**, 10258 (2014).
19. F. Stickel, E.W. Fischer, R. Richert, J. Chem. Phys. **102**, 6251 (1995).
20. J.C. Martinez-Garcia, J. Martinez-Garcia, S.J. Rzoska, J. Hulliger, J. Chem. Phys. **137**, 064501 (2012).
21. V.N. Novikov, A.P. Sokolov, Phys. Rev. E **92**, 062304 (2015).
22. Y.S. Elmatad, D. Chandler, J.P. Garrahan, J. Phys. Chem. B **113**, 5563 (2009).
23. R. Casalini, M. Paluch, C.M. Roland, J. Chem. Phys. **118**, 5701 (2003).
24. R. Casalini, C.M. Roland, Phys. Rev. Lett. **92**, 245702 (2004).
25. W. Götze, *Complex Dynamics of Glass-Forming Liquids: A Mode-Coupling Theory* (Oxford University Press, 2008).
26. W. Kob, S. Roldán-Vargas, L. Berthier, Nat. Phys. **8**, 164 (2012).
27. L. Berthier, G. Biroli, D. Coslovich, W. Kob, C. Toninelli, Phys. Rev. E **86**, 031502 (2012).
28. G. Biroli, J. Bouchaud, *The random first order transition theory of glasses: A critical assessment*, in *Structural Glasses and Supercooled Liquids* (Wiley-Blackwell, 2012) Chapt. 2, p. 31.
29. T. Rizzo, T. Voigtmann, EPL **111**, 56008 (2015).
30. T. Rizzo, Phys. Rev. B **94**, 014202 (2016).
31. W. Kob, H.C. Andersen, Phys. Rev. E **51**, 4626 (1995).

32. E. Flenner, G. Szamel, Phys. Rev. E **73**, 061505 (2006).
33. S.S. Ashwin, S. Sastry, J. Phys.: Condens. Matter **15**, S1253 (2003).
34. B. Doliwa, A. Heuer, Phys. Rev. E **67**, 031506 (2003).
35. K. Hukushima, K. Nemoto, J. Phys. Soc. Jpn. **65**, 1604 (1996).
36. S. Plimpton, J. Comput. Phys. **117**, 1 (1995).
37. LAMMPS: Large-scale Atomic/Molecular Massively Parallel Simulator, `http://lammps.sandia.gov/`.
38. R. Yamamoto, W. Kob, Phys. Rev. E **61**, 5473 (2000).
39. D. Frenkel, B. Smit, *Understanding Molecular Simulation: From Algorithms to Applications*, Vol. **1** (Academic Press, 2001).
40. atooms-pt: Multi-core/multi-GPU parallel tempering, `https://doi.org/10.5281/zenodo.1183663`.
41. N. Bailey, J.S. Hansen, T. Ingebrigtsen, A. Veldhorst, L. Bohling, C. Lemarchand, A. Olsen, A. Bacher, L. Costigliola, U. Pedersen *et al.*, SciPost Phys. **3**, 038 (2017).
42. atooms: A python framework for simulations of interacting particles, `https://doi.org/10.5281/zenodo.1183301`.
43. mpi4py, `http://mpi4py.scipy.org/docs/`.
44. L. Berthier, W. Kob, J. Phys.: Condens. Matter **19**, 205130 (2007).
45. C. Donati, S. Franz, S.C. Glotzer, G. Parisi, J. Non-Cryst. Solids **307**, 215 (2002).
46. T. Kawasaki, H. Tanaka, Proc. Natl. Acad. Sci. U.S.A. **107**, 14036 (2010).
47. H. Tanaka, Eur. Phys. J. E **35**, 113 (2012).
48. S. Toxvaerd, U.R. Pedersen, T.B. Schroder, J.C. Dyre, J. Chem. Phys. **130**, 224501 (2009).
49. T.S. Ingebrigtsen, J.C. Dyre, T.B. Schroder, C.P. Royall, *Crystallisation instability in glassforming mixtures*, arXiv:1804.01378 (2018).
50. F.H. Stillinger, T.A. Weber, Phys. Rev. A **25**, 978 (1982).
51. J.D. Honeycutt, H.C. Andersen, J. Phys. Chem. **91**, 4950 (1987).
52. L.O. Hedges, R.L. Jack, J.P. Garrahan, D. Chandler, Science **323**, 1309 (2009).
53. M. Newman, *Networks: An Introduction*, 1st edition (Oxford University Press, Oxford, New York, 2010).
54. G. Odriozola, L. Berthier, J. Chem. Phys. **134**, 054504 (2011).
55. Y. Rosenfeld, P. Tarazona, Mol. Phys. **95**, 141 (1998).
56. T.S. Ingebrigtsen, A.A. Veldhorst, T.B. Schroder, J.C. Dyre, J. Chem. Phys. **139**, 171101 (2013).
57. D. Coslovich, Phys. Rev. E **83**, 051505 (2011).
58. F. Turci, C.P. Royall, T. Speck, Phys. Rev. X **7**, 031028 (2017).
59. W. Kob, D. Coslovich, Phys. Rev. E **90**, 052305 (2014).
60. S. Sastry, P.G. Debenedetti, F.H. Stillinger, Nature **393**, 554 (1998).
61. A. Hudson, K.K. Mandadapu, *On the nature of the glass transition in atomistic models of glass formers*, arXiv:1804.03769 (2018).
62. V.N. Novikov, A.P. Sokolov, Phys. Rev. E **67**, 031507 (2003).
63. K. Kim, R. Yamamoto, Phys. Rev. E **61**, R41 (2000).
64. L. Berthier, G. Biroli, J.-P. Bouchaud, W. Kob, K. Miyazaki, D.R. Reichman, J. Chem. Phys. **126**, 184504 (2007).
65. E. Flenner, G. Szamel, J. Chem. Phys. **138**, 12A523 (2013).
66. S. Karmakar, C. Dasgupta, S. Sastry, Proc. Natl. Acad. Sci. U.S.A. **106**, 3675 (2009).
67. L. Berthier, G. Biroli, J.P. Bouchaud, W. Kob, K. Miyazaki, D.R. Reichman, J. Chem. Phys. **126**, 184503 (2007).
68. C.P. Royall, A. Malins, A.J. Dunleavy, R. Pinney, J. Non-Cryst. Solids **407**, 34 (2015).
69. J.C. Dyre, Rev. Mod. Phys. **78**, 953 (2006).
70. S. Mirigian, K.S. Schweizer, J. Chem. Phys. **140**, 194506 (2014).
71. M.H. Cohen, G.S. Grest, Phys. Rev. B **20**, 1077 (1979).
72. Y.S. Elmatad, D. Chandler, J.P. Garrahan, J. Phys. Chem. B **114**, 17113 (2010).
73. D. Gazzillo, G. Pastore, Chem. Phys. Lett. **159**, 388 (1989).
74. P. Sindzingre, C. Massobrio, G. Ciccotti, D. Frenkel, Chem. Phys. **129**, 213 (1989).
75. T.S. Grigera, G. Parisi, Phys. Rev. E **63**, 045102 (2001).
76. A. Ninarello, L. Berthier, D. Coslovich, Phys. Rev. X **7**, 021039 (2017).
77. L. Berthier, D. Coslovich, A. Ninarello, M. Ozawa, Phys. Rev. Lett. **116**, 238002 (2016).